IET Science, Measurement & Technology

Research Article

IET Journals
The Institution of Engineering and Technology

Performance analysis of epoxy nanocomposites due to water droplet-initiated discharges under AC and DC voltages and localisation of discharges

ISSN 1751-8822
Received on 15th March 2018
Revised 29th July 2018
Accepted on 3rd October 2018
E-First on 5th November 2018
doi: 10.1049/iet-smt.2018.5056
www.ietdl.org

Palash Mishra[1], B.M. Ashwin Desai[1], Ramanujam Sarathi[1] ✉, Takahiro Imai[2]

[1]*Department of Electrical Engineering, Indian Institute of Technology Madras, Chennai 600036, India*

[2]*Toshiba Corporation, Power and Industrial Systems R&D Centre, 1, Toshiba-cho, Fuchu-shi, Tokyo, 183–8511, Japan*

✉ *E-mail: rsarathi@iitm.ac.in*

Abstract: Corona inception voltage (CIV) due to water droplet sitting over the surface of epoxy nanocomposite material depends on supply voltage frequency, the conductivity of water droplet and the contact angle of the test specimens. The contact angle of the specimen and CIV due to water droplet has a direct correlation. It is realised that the CIV is high under negative DC and the least under AC voltages. Surface charge accumulation studies indicate that the accumulated charge and its decay time constant reduces in the damage-caused zone due to corona activity. The ultra-high frequency (UHF) signal generated due to water droplet-initiated corona activity has frequency content in the range of 0.8–1 GHz. The localisation of incipient discharges is demonstrated by using the non-iterative technique and the cross recurrence plot (CRP) technique is used to estimate the time difference of arrival (TDOA) of UHF signals generated due to water droplet-initiated discharge. Laser-induced breakdown spectroscopy (LIBS) depicts the elemental composition and reveals the difference in plasma temperature and threshold fluence between all the test specimens. In short, the performance of ion trapping particle filled epoxy nanocomposite performance is found to be best followed by titania filled epoxy nanocomposite and the base epoxy resin.

1 Introduction

With the advancement in nanotechnology, it has become easier for insulation designers to achieve the desired properties of the insulating material for power apparatus, with high performance. Epoxy resin and its composites are gaining considerable importance in electrical applications such as bushings, spacers, cable terminations, machine insulations etc., because of their inherent properties such as light weight, high density, low wettability, viscosity with excellent thermal endurance and a cost-effective material [1–3]. In addition, as compared to their counterpart microcomposites epoxy nanocomposites have better electrical properties such as improved conductivity, permittivity, dielectric loss, and breakdown strength [1, 4, 5].

The addition of metal oxide particle to the base epoxy polymer is preferred by the researchers rather than using micrometric metal particle as a filler. Common practice is to use alumina, silica, titania, magnesia, clay etc. [6, 7].

Thabet *et al.* have formulated a mathematical equation to calculate the dielectric constant of the material with a different volume fraction of nanofillers with different polymer materials [8]. The deposition of discrete water droplets due to the wetting mechanisms such as rain or condensation of fog etc. over the surface of polymeric insulators such as epoxy leads to the local electric field intensification at the triple junction existing between insulating surface, water droplet, and surrounding air, causing the corona discharge, surface deterioration, and eventually the failure of an insulator [9]. Thus it is essential to understand the voltage at which the water droplet (of different conductivities) initiates discharges, which is called as corona inception voltage (CIV), under AC, DC, and under high-AC voltages of different frequencies. Sarathi *et al.* have studied the characteristics of the current pulse initiated due to the water droplet under DC fields and have concluded that the corona-injected current pulses have a rise time of few nanoseconds radiating ultra-high frequency (UHF) signals [10].

Titania-filled epoxy nanocomposites have shown increased hardness, improved resistance to partial discharges, reduced surface roughness, and increased treeing lifetime [11–13]. However, the studies on the effects of addition of inorganic ion exchangers (such as zirconium phosphate) on the base epoxy resin are scanty. Inorganic ion exchangers have superior ion trapping properties, high heat and oxidation resistance and thus they can be used in the insulation structure to improve its reliability [14]. Also, the impact of corona ageing and water droplet-initiated discharge studies with titania and ion trapping particle such as zirconium phosphate (inorganic functional material) filled epoxy resin are scanty. Hence, an attempt has been made in the present study to obtain considerable database by carrying out a methodical experimental study, to understand the impact of titania and ion trapping particle on the electrical properties of the epoxy resin.

Du *et al.* studied the effects of TiO_2 nanoparticles on the surface charge of the epoxy nanocomposites and suggested that charge dynamics is dependent upon the localised surface state which gets altered on the addition of nanoparticles [15]. Wu *et al.* studied the distribution of space charge in polymer nanocomposite material, which depends upon the property of nano-additive such as its size [16]. Thus, a considerable amount of research has been carried out to understand the use of titania filler on the dielectric performance of epoxy resin [13–17]. However, studies on the impact of the ion-trapping particle of nanometric size as filler material in epoxy resins, its impact on the surface properties and dielectric properties of the material are scanty. Also, the studies on the impact titania and ion-trapping agent on water droplet-initiated discharges are limited hence the database need to be acquired.

Laser-induced breakdown spectroscopy (LIBS) is one of the sophisticated techniques to determine the elemental composition of the material. The sensitivity to identify multi-elements in one shine of laser impingement is high. Also, LIBS is basically a type of non-destructive test. The amount of damage caused to the material surface during the LIBS study is very small [18, 19]. It can be used as an effective tool to identify the elemental composition of the insulating material at every stage of its ageing, to understand the characteristic variations of the material.

Water droplet-initiated discharges act as a precursor to tracking erosion of the insulator surface which can lead to a complete breakdown of the insulation. The magnitude of current injected

Table 1 Sample composition

Sample Acronym	Composition by weight%
S1	base epoxy resin
S2	Epoxy resin with the ion trapping particle (hydrotalcite compound modified with zirconium phosphate) (of 2 wt.%)
S3	Epoxy resin with titania nanoparticle (of 5 wt.%)

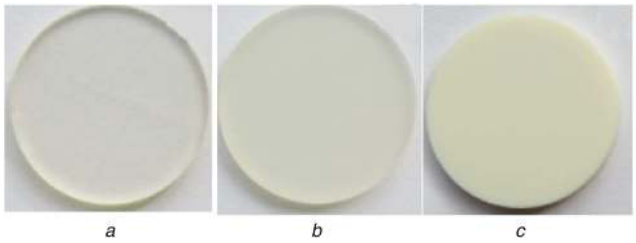

Fig. 1 *Typical photograph of virgin specimens*
(a) S1, ***(b)*** S2, ***(c)*** S3

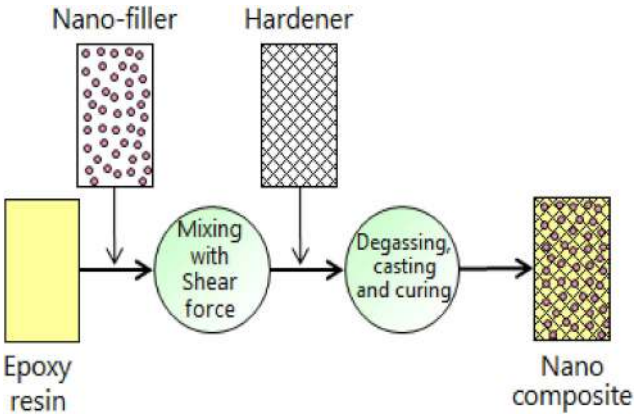

Fig. 2 *Schematic representation of procedural steps adopted with the preparation of epoxy nanocomposites*

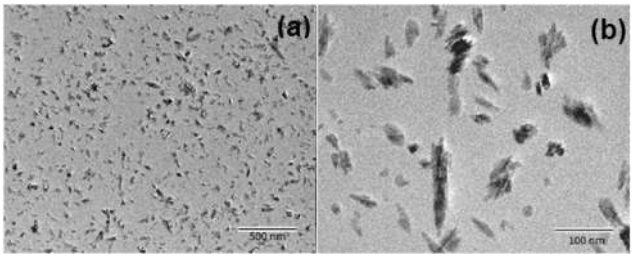

Fig. 3 *TEM picture of epoxy titania nanocomposites with different magnifications*
(a) 500 nm, ***(b)*** 100 nm

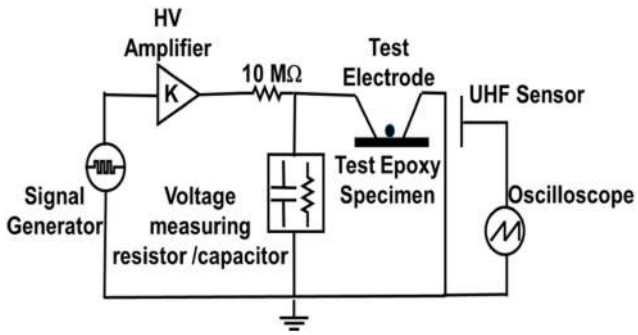

Fig. 4 *Experimental set-up for water droplet-initiated discharge studies*

during water droplet-initiated discharges is of few microamperes and it is difficult to detect these discharges just by measuring the leakage current [20]. Therefore it is necessary to identify and localise such discharges at a very primitive stage to prevent any catastrophic failure. One of the condition monitoring tools to identify such discharges is to use video surveillance and image processing techniques [21]. Thus an attempt has been made to demonstrate that the UHF technique allows one to identify the formation of discharges and to localise.

Recently, Bot *et al.* have employed the cross recurrence plot (CRP) technique for the estimation of time difference of arrival (TDOA) of underwater acoustic signals [22]. In the present study, an attempt has been made to localise the water droplet-initiated discharges by adopting CRP for estimating the TDOA of UHF signals formed due to water droplet-initiated discharges.

Having known all the above facts, the following methodical experimental studies were carried out to understand the performance of TiO_2 (titania) and ion-trapping agent IXEPLAS$_R$ (hydrotalcite compound modified with zirconium phosphate) filled epoxy nanocomposites to water droplet-initiated discharge studies: (i) variation in CIV initiated due to water droplet of different conductivity under AC, DC, and high-frequency AC voltages; (ii) variation in the surface charge decay characteristic of the epoxy nanocomposite material after corona ageing; (iii) analysis of surface charge distribution along the length of test samples with water droplet; (iv) analysis of UHF signal radiated during water droplet-initiated discharges; (v) analysis of material properties adopting LIBS; (vi) localisation of water droplet-initiated discharges using CRP for estimating TDOA.

2 Experimental setup and studies

2.1 Experimental setup

The different samples used for the study are listed in Table 1 and their typical photographs are shown in Fig. 1. Standard shearing, mixing, degassing, and curing procedures were used to prepare samples with epoxy as a base matrix [23]. The schematic representation of the procedural steps adopted for the preparation of epoxy nanocomposites is shown in Fig. 2.

Fig. 3 shows transmission electron microscopy (TEM) picture of epoxy titania nanocomposites (S3) with different magnification. For epoxy resin with ion trapping particle (S2), particles could not be observed in TEM images as its weight percentage is too low. The thin film for TEM studies was prepared by using a focused ion beam (model np FB2200, Hitachi Hi-Technologies Corporation, Japan) and uniform distribution of nanofillers in nanocomposites was visualised using a field emission transmission electron microscope (model no. HF-2200, Hitachi Hi-Technologies Corporation, Japan).

The ion-trapping particles having 500 nm average diameter and spherical shape, and TiO_2 particles having 15 nm average diameter and needle-like shape as shown in Fig. 3 were used in this study. The addition of nanofillers is to achieve the desired properties.

The experimental setup used for understanding water droplet-initiated discharge is shown in Fig. 4. The high DC and AC voltages of different frequencies are produced by use of a Trek amplifier (Model 20/20C) with input from a signal generator (Tektronix 3051C). For generated AC voltage measurement, a capacitive divider is used and for DC voltage measurement, a resistive divider is used. The voltage to the test specimens was increased at the rate of 200 V/s.

The test electrode arrangement comprises two stainless steel electrodes with its tip cut at 45° (according to IEC 60112 [24] set on a 3 mm thick epoxy composite material). The electrodes are separated by a gap distance of 10 mm as shown in Fig. 4. One electrode is connected to the high-voltage source through a current limiting resistor of 10 MΩ and the other electrode connected to ground. 10 µl of deionised water and 0.1 N NH_4Cl solution of different conductivities were used as a droplet.

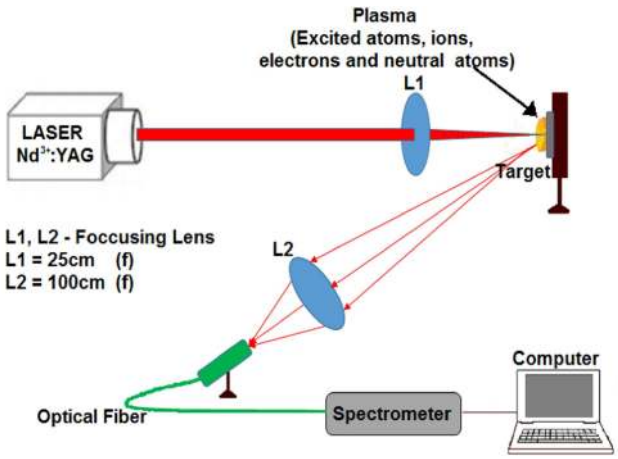

Fig. 5 *LIBS experimental set-up*

In the present study, a non-directional broadband UHF sensor was used by keeping the sensor at a distance of 20 cm from the water droplet-initiated discharge test setup. The output of the UHF sensor signal was measured using a high-bandwidth digital storage oscilloscope (LeCroyWavepro 7300A, 3.5 GHz bandwidth, operated at 20 GSa/s).

The corona was produced by using a high-frequency damped sinusoidal AC voltage of 15 kV. Samples were cut into 3 cm × 3 cm and were placed under the electrode with a 2 mm gap. In the present study, the specimens were exposed to corona treatment for 10 and 20 min and immediately subjected to studies.

2.2 Experimental studies

2.2.1 Surface charge measurement: Needle plane configuration was used to spray charges on the composite by generating corona at 12 kV +DC and −DC. The surface charge accumulation in epoxy composites after corona aging was measured using an electrostatic voltmeter (ESV) (Trek model 341B). The study was conducted with a deionised water droplet. The sensor measures the deposited charge present in 5 mm radius when it is placed 3 mm above the water droplet placed on the surface of the specimen.

The charge Q measured on the surface of the epoxy composite material is

$$Q = \frac{V \cdot \varepsilon_{\mathrm{o}} \cdot \varepsilon_{\mathrm{r}} \cdot A}{d}, \tag{1}$$

where A is the area of the curved surface of the sensor. d is the distance between the sensor surface and specimen. V is the voltage measured by an ESV. ε_{o} and ε_{r} are the permittivity of free space and relative permittivity of the specimen, respectively.

2.2.2 Laser-induced breakdown spectroscopy (LIBS): LIBS is a type of atomic emission spectroscopy, which uses a highly energetic laser pulse as the excitation source. The laser is focused to form plasma, which atomises and excites samples. The formation of the plasma only begins when the focused laser achieves a certain threshold for the optical breakdown, which generally depends on the environment and the target material. In principle, LIBS can analyse any matter regardless of its physical state, be it solid, liquid or gas. If the constituents of a material to be analysed are known, LIBS may be used to evaluate the relative abundance of each constituent element or to monitor the presence of impurities. In the present study, Nd3 + YAG laser was focused on the sample using 25 cm focal length and guided to the spectrometer (Ocean Optics) through the multimode optical fibre of core diameter 400 µm, 0.22NA as shown in Fig. 5. An integration period of 1 s was used to obtain spectra.

2.3 Localisation of discharges

2.3.1 Cross recurrence plot: CRP is a bi-variable version of recurrence plot [25, 26]. CRP is an effective graphical method to determine the time instant at which state space trajectory of one signal visits the close by a zone of state space trajectory of another signal. This method effectively determines the similarity in the two dynamical frameworks with the related lag/lead. Hence the CRP method can be employed to estimate the TDOA of signals. The following steps are involved in the construction of CRP of two signals.

Step 1: Phase space trajectory construction of two signals (x and y) using the time delay embedding method [27].

$$\boldsymbol{x_m}(i) = [x(i),\ x(i+\tau),\ \ldots, x(i+(m-1)\tau)], \tag{2}$$

$$\boldsymbol{y_m}(j) = [y(j),\ y(j+\tau), \ldots, y(j+(m-1)\tau)], \tag{3}$$

where $i = \{1, 2,\ldots, Nx-(m-1)\tau\}, j = \{1, 2,\ldots, Ny-(m-1)\tau\}$, where τ is the embedding delay (not TDOA), m is the embedding dimension, $N_x = N_y = N$ is the number of samples of signals x and y.

Step 2: Measurement of the degree of closeness of states of two space trajectories. This gives $N \times N$ similarity matrix

$$d(i,j) = \mathrm{Sim}(\ \boldsymbol{x_m}(i), \boldsymbol{y_m}(j)\ ), \tag{4}$$

where Sim (similarity function) can be a variety of mathematical functions, which can be used to measure the degree of closeness of states, such as Euclidean norm, dot product, and Pearson's correlation coefficient [22, 28]. In this study, dot product has been used as similarity function as it is found to be more appropriate for measuring the closeness of states [26].

Step 3: The CRP matrix is obtained from the similarity matrix by comparing each entry of the matrix with a threshold ϵ

$$\mathrm{CRP}(i,j) = H(\mathrm{Sim}(\ \boldsymbol{x_m}(i), \boldsymbol{y_m}(j)\ ) - \epsilon, \tag{5}$$

where $H(\ )$ is the Heaviside function. Therefore, when two states are close (within a threshold) CRP entry takes a value of 1, or else it takes a value of 0. In our case, ϵ was chosen to be 10% of the maximum value of the dot product of vectors. This choice was found to be very apt as ϵ the threshold is not fixed, but varies with two signals being compared in this way ϵ is also dynamic. Also embedding dimension m was chosen as 3 with unit delay embedding ($\tau = 1$), as a three-dimensional trajectory is clearer to visualise and delay of one is found to work fine and is in accordance with the guidelines to choose m and τ [29].

2.3.2 Recurrence quantification analysis (RQA): CRP, gives visual information about signal similarities and associated lag. However, in order to quantitatively determine lag for estimating TDOA, RQA is done on the CRP matrix [22]. In this study, sum of similarity (SS) metric is used for calculating TDOA of UHF signals and is defined a

$$\mathrm{SS}(t) = \begin{cases} \displaystyle\sum_{i=1}^{N+t} \mathrm{CRP}(i-t, i) \odot dd(i-t, i)\ \ (t<0), \\ \displaystyle\sum_{i=1}^{N-t} \mathrm{CRP}(i, i+t)\ \odot dd(i, i+t)\ \ (t \geq 0)\ , \end{cases} \tag{6}$$

where $\odot$ is the Hadamard product. The TDOA is measured as

$$\mathrm{TDOA} = t \text{ such that } \arg\max_{t}\ (\mathrm{SS}(t))\ . \tag{7}$$

When both signals of the CRP have a similar waveform with certain delay t then the RQA measurements will have a maximum diagonal value.

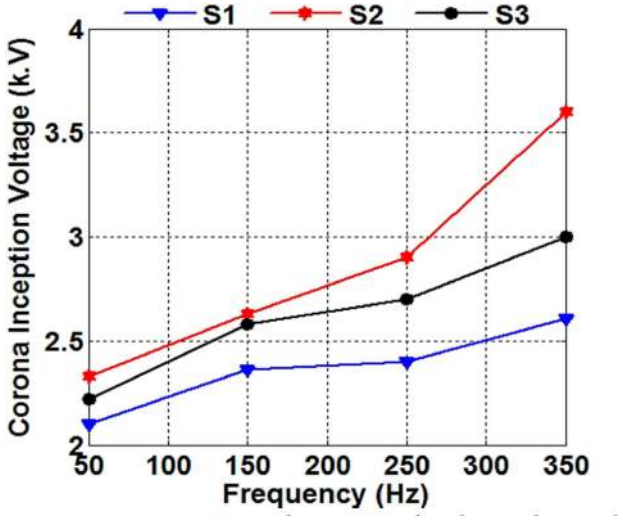

Fig. 6 *Variation in CIV due water droplet with supply voltage frequency*

2.3.3 Source localisation: Let the partial discharge source be located at some point (x, y, z) and four sensors be located at known positions S1(x_1, y_1, z_1), S2(x_2, y_2, z_2), S3(x_3, y_3, z_3), and S4(x_4, y_4, z_4), and the entire space is considered within the positive axis of all coordinates

$$(x - x_1)^2 + (y - y_1)^2 + (z - z_1)^2 = (vT)^2, \tag{8}$$

$$(x - x_2)^2 + (y - y_2)^2 + (z - z_2)^2 = (v(T + \tau_{12}))^2, \tag{9}$$

$$(x - x_3)^2 + (y - y_3)^2 + (z - z_3)^2 = (v(T + \tau_{13}))^2, \tag{10}$$

$$(x - x_4)^2 + (y - y_4)^2 + (z - z_4)^2 = (v(T + \tau_{14}))^2, \tag{11}$$

where v is the velocity of the electromagnetic signal, T is the time of propagation of the signal from the source to sensor 1. τ_{12}, τ_{13}, and τ_{14} are propagation delays between sensor 1 and sensor 2, sensor 3 and sensor 4, respectively. This equation system (8)–(11) can be solved non-iteratively to find source location [30]. In the present study, CRP is used to estimate propagation delay between sensors, further obtained TDOAs are validated [31] and water droplet-initiated discharges are localised.

2.3.4 UHF signal simulation: The CRP method is also verified on simulated UHF signals. The UHF signal is generated as a double exponential signal [32]. White Gaussian noise is added to the UHF signal to obtain the required signal-to-noise ratio (SNR). The UHF signal $v(t)$ is defined as

$$v(t) = K(e^{(-1.3t/\tau)} - e^{(-2.2t/\tau)})\sin(2\pi f_c t), \tag{12}$$

where K is the amplitude of the UHF signal, f_c is the frequency of the signal and τ is the shaping parameter. In the present work, A, f_c, and τ are assumed to be 40 mV, 1000 MHz and 1 ns, respectively [32].

3 Results and discussion

3.1 Analysis of variation in CIV due to water droplet

The CIV was determined based on the first UHF signal generated by water droplet-initiated discharges within the electrode gap due to the applied voltage. Fig. 6 shows the variation in CIV due to the deionised water droplet, under high-frequency AC voltages. It is observed that CIV increases with an increase in supply voltage frequency. Nazemi *et al.* [9] have clearly observed that there exist different modes of oscillation of water droplet sitting on the surface of the sample. Under AC stress, water droplet elongates at the edges, along with the axis of the electrodes which results in electric field intensification at the triple junction of the surface, water, and air. Hence corona inception takes place. At a higher frequency of supply voltage, the water droplet oscillates more and the stretching of the water droplet is less as compared to that at lower frequencies requiring higher voltage for corona to incept.

To understand the impact of the conductivity of water droplet on corona inception, 0.1 N NH_4Cl solution of different conductivities is used. From Fig. 7 it is observed that with the increase in the conductivity of water droplet, a reduction in CIV takes place, under AC and DC voltages. The reason behind this is that the water droplet gets polarised due to the applied electrical stress. With the increase in conductivity this polarisation increases, resulting in higher stress at the triple junction between water, air, and insulator surface, hence conductivity has an inverse relationship with CIV. It is also noticed that the CIV is higher under negative DC voltage as compared to AC and positive DC voltages. The values of CIV obtained are within the error of ±0.05 kV. Comparing the material performance of the test specimens using CIV, it is observed that CIV follows the sequence S1 < S3 < S2, under AC and DC voltages. The reason behind this is the variation in their contact angle, as shown in Table 2, which follows the order S1<S3<S2. The contact angle has a direct relationship with CIV. If the contact angle is higher the spread of water droplet is less along the axis of the electrode, increasing the effective mean distance between the high- and the low-voltage electrode. Hence resulting in higher CIV. Hence it can be concluded that sample S2 with the highest CIV performs better than other samples.

3.2 Impact of corona ageing on contact angle and CIV

One of the basic processes by which the power apparatus insulation degrades is corona activity. Therefore it is essential to identify the material with good discharge resistance. Analysis of the contact angle of the surface after corona ageing gives information about the level of surface degradation due to corona ageing.

Fig. 8 shows the variation in contact angle of the epoxy nanocomposite material post corona ageing. On corona ageing, a drastic reduction in contact angle is observed, irrespective of the type of epoxy material/nanocomposite under test. The measurement of the contact angle is within the error of ±5°. It is observed that for the virgin specimens the contact angle is highest for S2 followed by S1 and S3. The same order is also observed with the corona-aged specimens. It is already mentioned in Section 3.1 that CIV and contact angle follow the direct relationship. Furthermore, the CIV follows the same order as the contact angle after corona ageing, indicating superior performance of S2 even after corona ageing as compared to S1 and S3.

The surface roughness of the corona-aged specimens was measured using a non-contact optical profilometer, as shown in Table 3. The surface roughness is not the same even though the duration of discharge exposure is the same for each specimen. It is observed that surface roughness follows the order S2<S3<S1 post corona ageing, indicating that the ion trapping particle mixed nanocomposite is least prone to surface erosion. Fig. 9 shows variation in CIV formed due to water droplet sitting on top of the corona-aged specimen. Considerable reduction in CIV is observed after corona ageing and the reduction in CIV is almost the same above a certain level of corona ageing. This characteristic is the same under AC and DC voltages.

On corona inception, the voltage is further increased for discharge activity to occur between the water droplet and the electrodes and the magnitude of voltage is maintained for 30 s to understand the level of damage to the insulating material. Fig. 10 shows a typical photograph of damage caused due to water droplet-initiated discharges. It is observed that the level of erosion is the smallest with S2 and maximum with S1 specimen. Also, the amount of erosion is high under DC voltage than under AC voltage.

Furthermore, the conductivity of the nanocomposites was measured by using a Novo control technology broadband dielectric/impedance spectrometer (Alpha-A high performance frequency analyser) is shown in Fig. 11. It is observed that the conductivity of ion trapping particle-filled epoxy nanocomposite (S2) is least followed by titania-filled epoxy nanocomposite (S3)

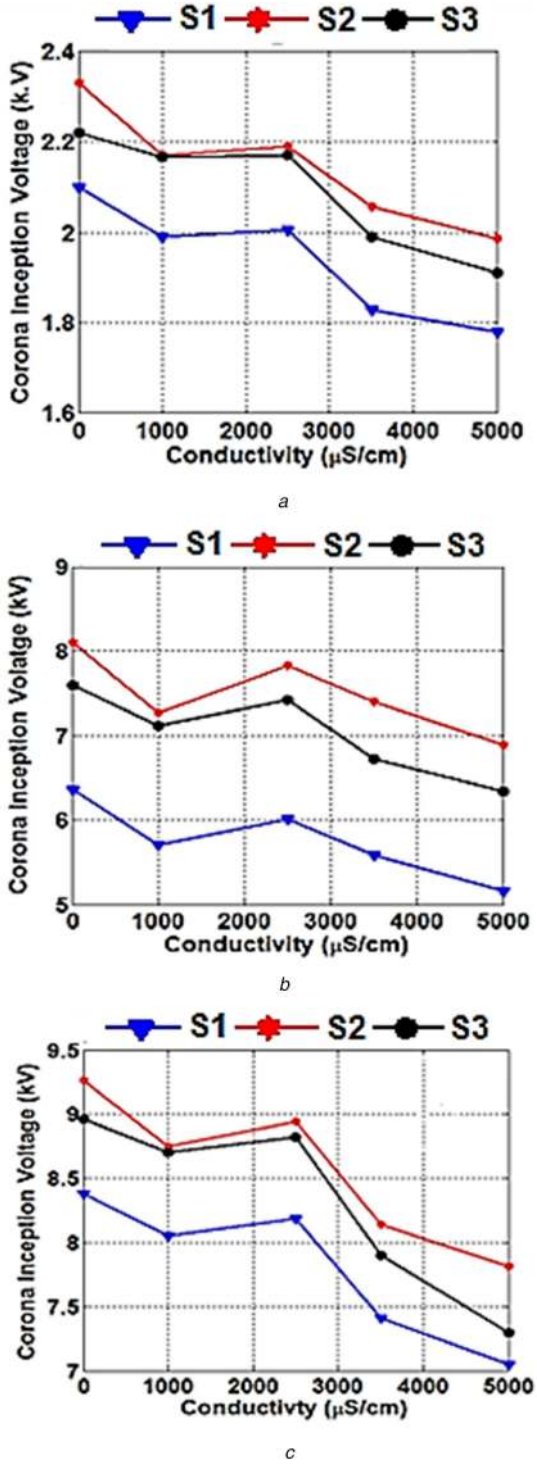

Fig. 7 *Variation in CIV with a conductivity of water droplet*
(a) AC, ***(b)*** +DC, ***(c)*** –DC

Table 2 Contact angle of virgin specimens

Sample	Contact angle, °
S1	69.55
S2	82.33
S3	76.74

and base epoxy resin (S1). In the process, the ion trapping filler limits the injection of current thereby limiting the discharge channel/amount of damage (Fig. 10) having high discharge resistant properties (S2) being superior to other composite materials (S1 and S3).

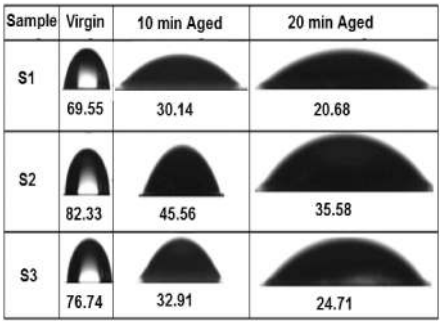

Fig. 8 *Typical photograph showing variation in contact angle on the corona-aged specimen*

Table 3 Variation in the mean surface roughness of corona aged specimens

Sample	Mean surface roughness, μm
S1	651.833 ± 5
S2	346.956 ± 5
S3	354.276 ± 5

3.3 Change in surface charge characteristics in the presence of water droplet

The surface condition of the insulating material has a high impact on the performance of the insulating material. The surface charge accumulation in insulating materials can initiate surface discharge activity which can cause damage to the insulating material. Fig. 12 shows the surface charge decay characteristics of virgin epoxy specimens and corona-aged epoxy specimens. The surface charge accumulation studies were carried out by depositing charges by the corona injection process under positive and negative DC voltage and then calculating the charge using (1). It is observed that the surface charge decay follows the exponential pattern and is given by

$$Q(t) = Q_0 e^{-\lambda t}, \tag{13}$$

where λ is the decay rate. Also, the mean life time 'τ' is calculated as $\tau = (1/\lambda)$. Table 4–6 show the initial charge stored and charge decay rate (λ) for the virgin, 10 min corona aged, and 20 min corona-aged epoxy specimens, respectively. It is observed that the decay rate gets drastically increased for the corona-aged specimens. From Fig. 12*a*, it is clear that the surface charge decay characteristic for all the virgin samples are almost the same with only a marginal difference in the decay rate and initial charge.

However, after the corona ageing (Figs. 12*b* and *c*), the magnitude of charge acquired and decay time constant reduces drastically. The reason is corona ageing significantly modifies the surface of the polymeric insulating material and lead to the generation of deep and shallow traps through which the charges detrap at a different rate [33–35]. Table 4 shows the initial charge and decay rate of virgin and corona-aged specimens. It is clearly observed that the decay rate is higher under negative polarity. The reason behind this is the higher mobility of electrons than the positive ions. The charge retention capability before and after corona ageing is highest for S2 and lowest for S1, irrespective of the polarity of charge injected. Thus the change in surface charge decay characteristics after corona ageing for the sample S2 is least and its performance is superior to other test specimens.

3.4 Potential distribution over the surface of the insulating material in the presence of water droplet

During operation, the water droplet on the surface of the insulating material can alter the local electric field [36]. Fig. 13 shows the characteristic variation in potential distribution over the surface of virgin and corona-aged epoxy/epoxy nanocomposites under test with the water droplet placed at the distance of 1.5 cm from either edge of test specimens. It is observed that the charge retention

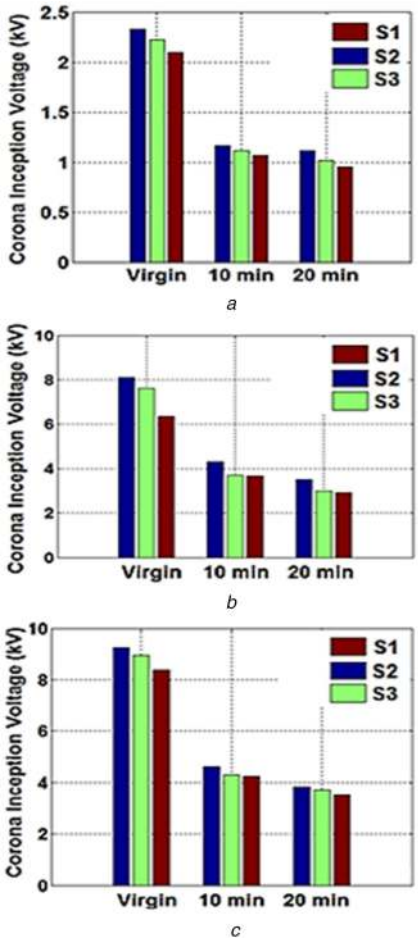

Fig. 9 *Variation in CIV after corona ageing under* ***(a)*** AC, ***(b)*** +DC, ***(c)*** −DC

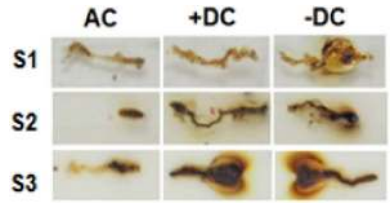

Fig. 10 *Typical photograph of epoxy nanocomposites due to water droplet-initiated discharges under AC and DC voltages*

capability of the samples reduces for the corona-aged specimen (Figs. 13*b* and *c*). The peaks of the potential distribution follow the order S2 > S3 > S1 for the virgin and corona-damaged specimens.

However, in the case of corona-aged specimens, the magnitude of surface potential reduces. Furthermore, the reduction in the surface potential peak value due to corona ageing is maximum for sample S1 and minimum for sample S2 indicating the superior performance of sample S2. Also from Fig. 13, it is observed that for the virgin specimens the peaks are sharp in nature as compared to corona-aged specimens where peaks become more of a smooth topped nature.

3.5 Analysis of UHF signal formed due to the water droplet-initiated discharges

A typical UHF signal generated due to water droplet sitting on epoxy nanocomposites initiated discharges is shown in Fig. 14. Figs. 15*a–c* show the fast Fourier transform (FFT) of the UHF signal generated due to corona activity and water droplet sitting on the top of epoxy nanocomposites, at the point of inception, under AC and DC voltages.

From Figs. 15*a–c*, it is clearly concluded that UHF signal formed due to corona discharge activity initiated by water droplet

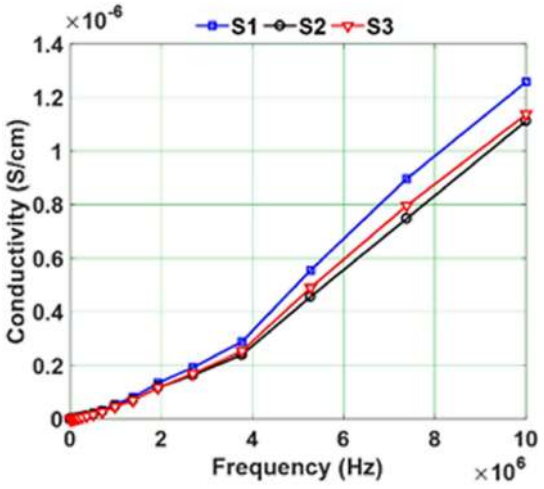

Fig. 11 *Variation in conductivity of epoxy nanocomposites with frequency*

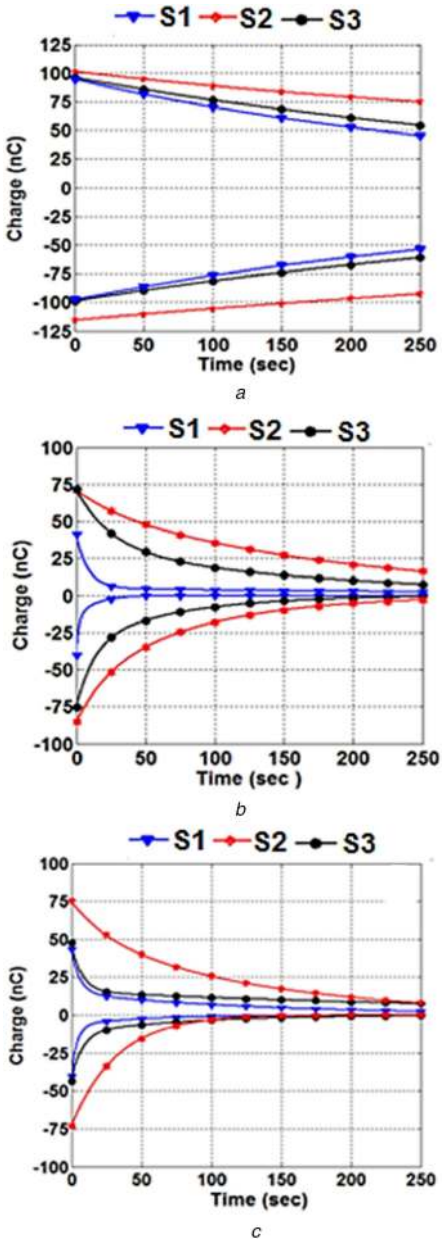

Fig. 12 *Surface charge decay characteristics for* ***(a)*** Virgin specimens, ***(b)*** 10 min corona-aged specimens, ***(c)*** 20 min corona-aged specimens under positive DC and negative DC corona charging

sitting on epoxy nanocomposites, under AC and DC voltages have a frequency in the range of 0.8–1 GHz. Under negative DC voltages, a marginal increase in the energy level observed in the low-frequency range. Not much variation is observed above 1 GHz.

Table 4 Initial charge and decay rate of virgin epoxy specimens

Sample	Positive DC		Negative DC	
	Initial charge, nC	Decay rate, τ	Initial charge, nC	Decay rate, τ
S2	99.22	0.00109	115.11	0.00131
S3	96.00	0.00123	98.93	0.00193
S1	94.25	0.00242	97.25	0.00290

Table 5 Initial charge and decay rate of 10 min corona-aged epoxy specimens

Sample	Positive DC		Negative DC	
	Initial charge, nC	Decay rate, τ	Initial charge, nC	Decay rate, τ
S2	74.9	0.0186	85.385	0.0148
S3	47.39	0.0300	74.375	0.0256
S1	43.52	0.0473	42.42	0.0492

Table 6 Initial charge and decay rate of 20 min corona-aged epoxy specimens

Sample	Positive DC		Negative DC	
	Initial charge, nC	Decay rate, τ	Initial charge, nC	Decay rate, τ
S2	74.9	0.0186	74.1	0.0241
S3	47.39	0.0300	46.6	0.0317
S1	43.52	0.0473	41.4	0.0501

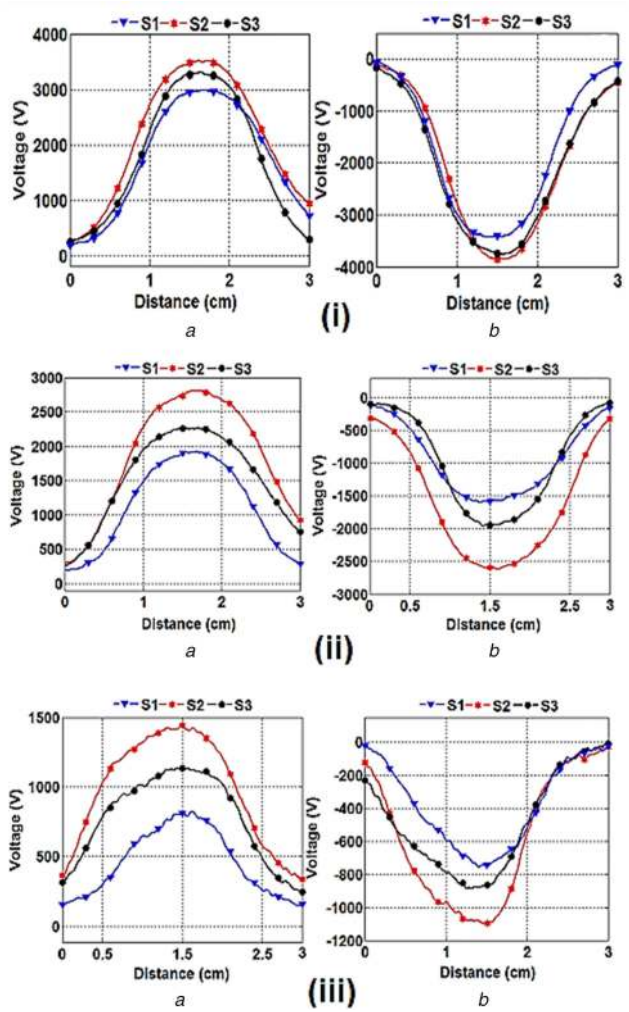

Fig. 13 *Variation in the potential distribution along the length of the epoxy specimen for (i)Virgin sample, (ii)10 min corona-aged samples, (iii) 20 min corona-aged samples under*
(a) +DC, ***(b)*** –DC fields

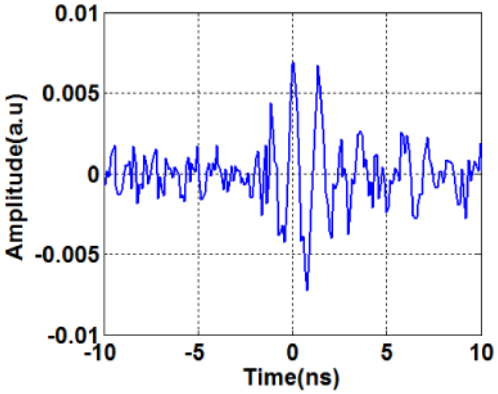

Fig. 14 *Typical time domain representation of UHF signal generated during the inception*

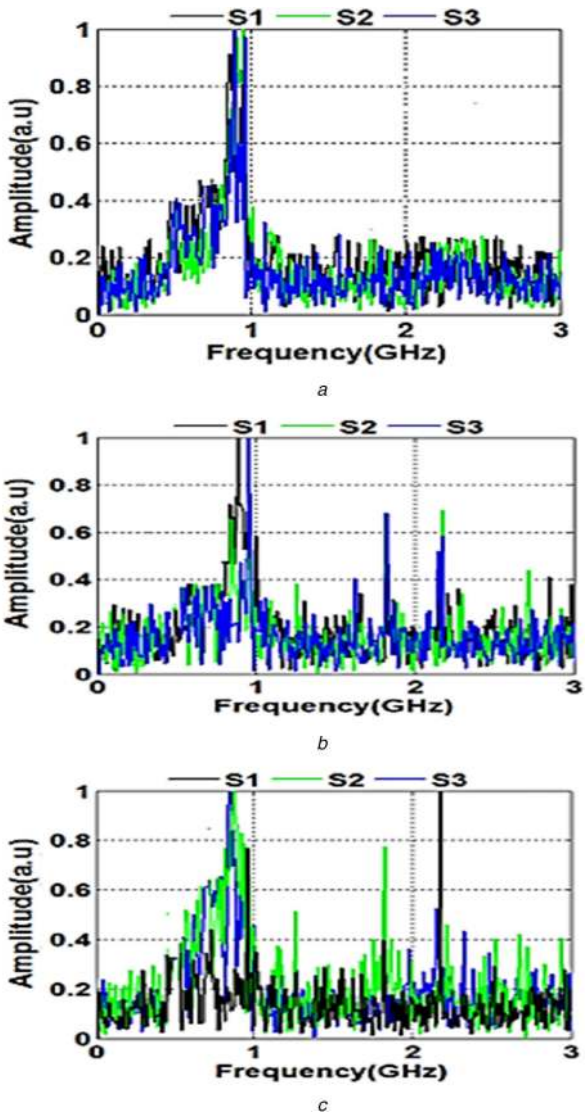

Fig. 15 *FFT analysis of the inception voltages for all the samples S1, S2, and S3 under*
(a) AC field, ***(b)*** +DC field, ***(c)*** −DC field

3.6 LIBS analysis and vicker hardness test

LIBS analysis for all the samples is performed for two main purposes. Firstly to detect the elemental composition and plasma temperature of all the resin and secondly to find the correlation between the plasma temperatures and micro vicker hardness. Meyer *et al.* have compared laser abrasion resistance and tracking tests and observed that laser erosion resistance can be used to rank the material easily [37]. Figs. 16*a–c* show the emission spectra of

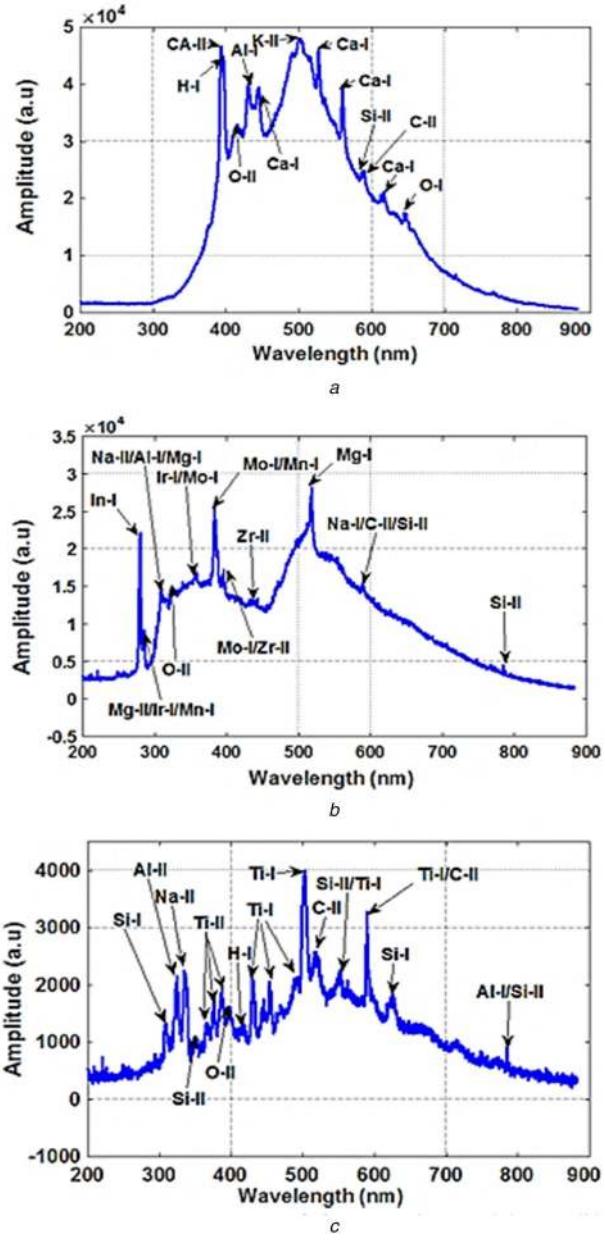

Fig. 16 *Emission spectra of the samples in*
(a) S1, ***(b)*** S2, ***(c)*** S3

S1, S2 and S3, respectively. In the emission spectra of S2, a few peaks of Zr are also observed. Similarly, in the S3, Ti peaks are observed because of the presence of the ion-trapping particle and TiO_2 nanoparticles.

Further plasma temperature is used to characterise the plasma produced by the ablation of materials through the interaction of the laser beam on the surface of the samples. The plasma temperature is calculated using the Boltzmann–Saha equation given by

$$T_e = 1.44\frac{E_2 - E_1}{\ln\left[\frac{I_1\,\lambda_1\,L_2\,g_2}{I_2\,\lambda_2\,L_1\,g_1}\right]}, \tag{14}$$

where E_1 and E_2 are excited energy levels, g_1 and g_2 are statistical weights of excited energy levels 1 and 2, respectively, L_1 and L_2 are transition probabilities of states, I_1 and I_2 are intensities of particular atomic species at λ_1 and λ_2 wavelength, respectively, and T_e is the plasma electron temperature under the condition of local thermodynamic equilibrium.

Table 7 shows the calculated plasma temperature using (14) for samples S1, S2 and S3. The Ca, Zr and Ti lines were used to calculate the plasma temperature of samples S1 S2 and S3,

Table 7 Variation in plasma temperature measured, laser fluence, and the hardness of epoxy nanocomposites

Sample	Plasma temperature	Hardness	Threshold fluence, mJ
S1	8289(Ca)	14.81 ± 0.3	11.83
S2	10,190(Zr)	24.25 ± 0.3	15.77
S3	9251(Ti)	19.26 ± 0.3	14.73

Table 8 Actual sensor and source locations

Sensor and source	P1(*x*,*y*,*z*), m	P2 (*x*,*y*,*z*), m
source	2.5, 5, 0.62	2.5, 5, 0.62
sensor 1	5, 2.5.0.62	1.5, 4, 0.62
sensor 2	4, 0, 0.62	4, 0, 0.62
sensor 3	1, 1, 0.62	5, 2.5, 0.62
sensor 4	1, 3.38, 0.62	1, 1.0.62

respectively [38]. It is observed that the plasma temperature follows the order S2 > S3 > S1. For all the samples, plasma temperature was obtained under identical conditions, at different locations on the sample and the average value is provided. Plasma temperature measured for the base epoxy resin and the composite material is different due to the inclusion of fillers. The inclusion of fillers causes variation in hardness levels of the material, which can be easily observed by variation in plasma temperature.

Table 7 also shows the micro vicker hardness for all the samples and it is found that the sample with higher plasma temperature has vicker hardness hence the mechanical hardness and plasma temperature (14) are directly proportional and plasma temperature can be used as an effective tool to estimate the surface hardness of the bulk material. Based on the results obtained for epoxy nanocomposites, correlating the surface roughness of the material due to corona discharge activity and surface plasma temperature formed indicates that material with higher plasma temperature has a higher hardness.

Furthermore, it has been reported in the literature that the ablation due to the erosion and depth of erosion of material due to high energy laser beam used during LIBS is less for the harder material [39, 40]. To quantify the erosion, the crater depth of all the samples is measured for a different number of shots of laser pulse ranging from 5 to 40 causing erosion of different depth as shown in Fig. 17. It is clear that the depth of the crater follows the order S1 > S3 > S2, again depicting the superior behaviour of S2. The typical 3D photograph of the crater formed by the laser pulse is shown Fig. 18.

3.7 Localisation of discharges

The localisation was done in an open air environment considering a coordinate system with a maximum distance between the source and sensor being 5.2 m. Table 8 shows the coordinates of the source and sensors. The entire system of the source and sensors is placed in an imaginary cube of 5 m. The localisation was done by keeping the sensors at two different positions (P1 and P2), and the technique was verified for both the positions.

CRP (6) was used to determine the TDOA (7) of UHF signals, the obtained TDOAs are correct up to the first decimal point (up to the resolution level) (Table 9). The obtained TDOAs were validated and the source is localised by the non-iterative method [29, 30]. A maximum deviation of 0.29 m was observed (Table 10) in localisation for the practical case, while in the simulation case, the maximum deviation was found to be 0.01 m. The cause for deviation in the practical case is because of limitation in the sampling rate of data acquired through an oscilloscope. An improved sampling in simulation case results in improved accuracy of localisation. While 0.01 cm deviation in the simulation case is because of noise introduced in the simulated signal with a SNR of −6 dB where the simulated signal was sampled at a resolution of 0.01 ns. The error in localisation is calculated as

$$e = \sqrt{(x - x_c)^2 + (y - y_c)^2 + (z - z_c)^2} \quad (15)$$

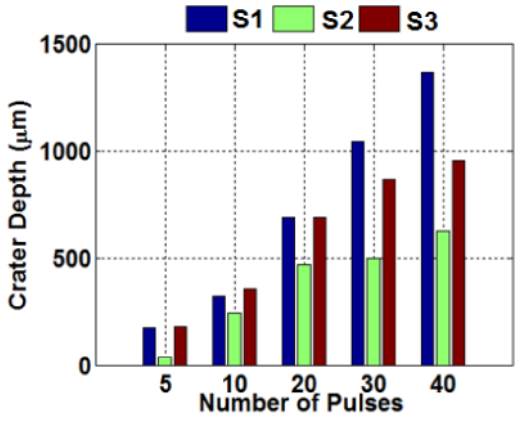

Fig. 17 *Variation of the depth of the crater with a number of laser pulses*

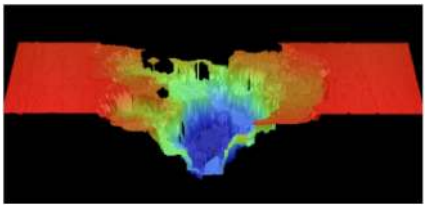

Fig. 18 *Typical 3D photograph of the crater formed by the laser pulse*

where x_c, y_c, and z_c are calculated source coordinates and x, y, and z are actual source coordinates. The error in the practical case (15) was around 0.25 m mainly because of the sampling rate, an improved sampling rate would definitely give better accuracy as can be seen in the simulation case (Table 11) (12).

4 Conclusions

The present study compares the performance of epoxy nanocomposites, filled with ion-trapping particle and titania filler, with the base epoxy resin. Corona discharge initiated due to water droplet sitting on epoxy nanocomposite increases with supply voltage frequency. Increase in conductivity of water droplet reduces the CIV. Surface roughness follows the inverse relationship with the contact angle and CIV. In the present study, it is found that the ion-trapping particle-filled epoxy nanocomposite has the highest contact angle and CIV, followed by titania-filled epoxy nanocomposite and base epoxy resin. The trend is similar in virgin as well as corona-aged specimens.

The amount of the surface damage caused to all the epoxy resins due to water droplet-initiated discharges is high under –DC voltage than + DC and AC voltage. Also, the surface damage, depth of erosion and carbonisation due to AC and DC voltages is maximum for the base epoxy resin and the least for the ion-trapping particle-filled epoxy nanocomposite.

Surface charge accumulation studies indicate that the accumulated charges decay fast for corona-aged specimens. The water droplet-initiated discharges under AC and DC voltages radiate a UHF signal whose frequency band lies in the range of 0.8 −1 GHz. CRP was used to estimate the TDOA of UHF signals. The obtained TDOA was validated and the source was localised, it was further observed that the improved sampling rate of the signal would give a better accuracy of localisation.

LIBS analysis provides the elemental composition of the epoxy nanocomposite material. The values of micro vicker hardness, threshold fluence and plasma temperature formed show the direct relationship. Ion-trapping particle has the highest plasma

Table 9 Actual and estimated TDOAs.

TDOA	Actual, ns		Calculated SS method, ns		Simulated, ns	
	P1	P2	P1	P2	P1	P2
τ_{12}	12.765	5.6518	12.7	5.6	12.76	5.65
τ_{13}	7.1128	2.4707	7.1	2.4	7.11	2.47
τ_{14}	9.5835	−5.2901	9.5	−5.3	9.58	−5.29

Table 10 Actual and estimated source locations

Method	P1 (x,y,z), m	P2 (x,y,z), m
actual location	2.5, 5, 0.62	2.5, 5, 0.62
practically calculated	2.48, 4.98, 0.38	2.47, 4.98, 0.33
calculated by simulation	2.50, 4.99, 0.61	2.50, 4.99, 0.61

Table 11 Root-mean-square error in the position of both the source practically and simulated

Position	Error practically, m	Simulation, m
P1	0.2416	0.014
P2	0.2922	0.014

temperature and hardness followed by titania-filled epoxy nanocomposite and base epoxy resin. The results of the study correlate well with the damage caused due to water droplet-initiated discharges.

In short, to conclude, the performance of base epoxy resin is strongly influenced and improved by the addition of nanoparticles. The ion-trapping particle-filled epoxy nanocomposite performs best among the test samples.

5 References

[1] Iyer, G., Gorur, R.S., Richert, R., *et al.*: 'Dielectric properties of epoxy based nanocomposites for high voltage insulation', *IEEE Trans. Dielectr. Electr. Insul.*, 2011, **18**, (3), pp. 659–666

[2] Lia, H., Du, B., Jin, L., *et al.*: 'Effects of non-linear conductivity on charge trapping and de-trapping behaviours in epoxy/SiC composites under DC stress', *IET Sci. Meas. Technol.*, 2017, **12**, (21), pp. 83–89

[3] Roy, M., Nelson, J.K., MacCrone, R.K., *et al.*: 'Polymer nanocomposites dielectrics—the role of the interface', *IEEE Trans. Dielectr. Electr. Insul.*, 2005, **2**, (4), pp. 629–641

[4] Iyer, G., Gorur, R.S., Krivda, A.: 'Understanding electrical discharge endurance of epoxy micro and nano composites through thermal analysis', *IEEE Trans. Dielectr. Electr. Insul.*, 2014, **21**, (1), pp. 225–229

[5] Tsekmes, I.A, Morshuis, P.H.F., Smit, J.J., *et al.*: 'Enhancing the thermal and electrical performance of epoxy microcomposites with the addition of nanofillers', *IEEE Electr. Insul. Mag.*, 2015, **31**, (3), pp. 32–42

[6] Singha, S., Thomas, M.J.: 'Dielectric properties of epoxy nanocomposites', *IEEE Trans. Dielectr. Electr. Insul.*, 2008, **15**, (1), pp. 12–23

[7] Kochetov, R., Andritsch, T., Morshuis, P.H.F., *et al.*: 'Anomalous behaviour of the dielectric spectroscopy response of nanocomposites', *IEEE Trans. Dielectr. Electr. Insul.*, 2012, **19**, (1), pp. 107–117

[8] Thabet, A.: 'Theoretical analysis for effects of nanoparticles on dielectric characterization of electrical industrial materials', *Electr. Eng. (ELEN) J.*, 2016, **99**, (2), pp. 487–493

[9] Nazemi, M.H., Hinrichsen, V.: 'Experimental investigations on partial discharge characteristics of water droplets on polymeric insulating surfaces at AC DC and combined AC–DC voltages', *IEEE Trans. Dielectr. Electr. Insul.*, 2015, **22**, (4), pp. 2261–2270

[10] Sarathi, R., Harsha, V.S., Vasa, N. J., *et al.*: 'Water droplet initiated discharges on epoxy nano composites under DC voltages', *IEEE trans. Dielectr. Electr. Insul.*, 2016, **23**, (3), pp. 1743–1752

[11] Tanaka, T., Imai, T.: '*Advanced nanodilectrics: fundamentals and applications*' (CRC Press, Florida, 2017), pp. 244–258

[12] Imai, T., Sawa, F., Ozaki, T., *et al.*: 'Influence of temperature on mechanical and insulation properties of epoxy-layered silicate nanocomposite', *IEEE Trans. Dielectr. Electr. Insul*, 2006, **13**, (2), pp. 445–452

[13] Kozako, M., Kido, R., Imai, T., *et al.*: 'Surface roughness change of epoxy/TiO2 nanocomposite due to partial discharges'. Proc. 2005 Int. Symp. on Electrical Insulating Material, Kitakyushu, Japan, 2005, vol. 3, pp. 661–664

[14] Wu, H., Liu, C., Chen, J., *et al.*: 'Preparation and characterization of chitosan/α-zirconium phosphate nanocomposite films', *Polym. Int.*, 2010, **59**, (7), pp. 923–930

[15] Du, B.X., Jhang, J.W., Gao, Y.: 'Effects of TiO_2 particles on surface charge of epoxy nanocomposites', *IEEE Trans. Dielectr. Electr. Insul.*, 2012, **19**, (3), pp. 755–762

[16] Jiandong, W., Wenhui, L., Yu, Z., *et al.*: 'Effect of nano additive size on the space charge behaviour in LDPE/SiO_2 nanocomposite'. Int. Conf. on Solid Dielectrics, Potsdam, Germany, 2010, pp. 1–4

[17] Maity, P., Basu, S., Parameswaran, V., *et al.*: 'Degradation of polymer dielectrics with nanometric metal-oxide fillers due to surface discharges', *IEEE Trans. Dielectr. Electr. Insul*, 2008, **15**, pp. 52–62

[18] Alexander, D.R., Poulain, D.E., Ahmad, M.U., *et al.*: 'Environmental monitoring of soil contaminated with heavy metals using Laser-induced breakdown spectroscopy'. Geoscience and Remote Sensing Symp., Palmerston North, New Zealand, 1994, Vol. 2, pp. 767–769

[19] DeLucia, F.C., Samuels, A. C., Harmon, R. S., *et al.*: 'Laser-induced breakdown spectroscopy (LIBS): a promising versatile chemical sensor technology for hazardous material detection', *IEEE Sens. J.*, 2005, **5**, (4), pp. 681–689

[20] Lapes, J.S., Jayaram, S.H., Cherney, E.A.: 'A study of partial discharges from water droplets on a silicone rubber insulating surface', *IEEE Trans. Dielectr. Electr. Insul.*, 2001, **8**, (2), pp. 262–268

[21] Murthy, V.S., Gupta, S., Mohanta, D.K.: 'Digital image processing approach using combined wavelet hidden Markov model for well-being analysis of insulators', *IET Image Process.*, 2011, **5**, (2), pp. 171–183

[22] Bot, O.L., Gervaise, C., Mars, J.: 'Time-difference-of-arrival estimation based on cross recurrence plots, with application to underwater acoustic signals', in Webber, C.L., Ioana, C., Marwan, N. (Ed.): '*Recurrence plots and their quantifications: expanding horizons (Springer Proceedings in Physics 180)*' (Springer, 2016), pp. 265–288

[23] Imai, T., Sawa, F., Ozaki, T., *et al.*: 'Evaluation of insulation properties of epoxy resin with nano-scale silica particles'. Proc. ISEIM, Kitakyushu, Japan, 2005, Vol. 1, pp. 239–242

[24] IEC 60 112.: 'Recommended method for determining the comparative tracking index of solid insulating material under the moist condition', 2nd Edition, 1972

[25] Zbilut, P., Giuliani, A., Webber, C.L., *et al.*: 'Detecting deterministic signals in exceptionally noisy environments using cross-recurrence quantification', *Phys. Lett. A*, 1998, **246**, (1–2), pp. 122–128

[26] Marwan, N., Romano, M.C., Thiel, M., *et al.*: 'Recurrence plots for the analysis of complex systems', *Phys. Rep.*, 2007, **438**, (5–6), pp. 237–329

[27] Packard, N.H., Crutchfield, J.P., Farmer, J.D., *et al.*: 'Geometry from a time series', *Phys. Rev. Lett.*, 1980, **45**, (9), pp. 712–716

[28] Bot, O.L., Gervaise, C., Mars, J.I., *et al.*: 'Similarity matrix analysis and divergence measures for statistical detection of unknown deterministic signals hidden in additive noise', *Phys. Lett. A*, 2015, **379**, (40–41), pp. 2597–2609

[29] Kundu, P., Kishore, N.K., Sinha, A.K.: 'A non-iterative partial discharge source location method for transformers employing acoustic emission techniques', *Appl. Acoust.*, 2009, **70**, (11–12), pp. 1378–1383

[30] Antony, D., Punekar, G.S.: 'Identification of invalid time-delay-groups using discriminant and Jacobian-determinant in acoustic emission PD source localisation', *IET Sci., Meas. Technol.*, 2017, **11**, (3), pp. 315–321

[31] Liu, Y., Zhou, W., Li, P., *et al.*: 'An ultrahigh frequency partial discharge signal de-noising method based on a generalized S-transform and module time-frequency matrix', *Sensors*, 2016, **16**, (6), p. 941

[32] Zhang, T., Luo, L., Hou, H., *et al.*: 'UHF signal model parameters identification and reconstruction for partial discharge in substation'. Int. Conf. on Condition Monitoring and Diagnosis (CMD), Xi'an, China, 2016, pp. 242–245

[33] Sjöstedt, H., Gubanski, S.M., Serdyuk, Y.V.: Charging characteristics of EPDM and silicone rubbers deduced from surface potential measurements', *IEEE Trans. Dielectr. Electr. Insul.*, 2009, **16**, 3 pp. 696–703

[34] Phillips, A.J., Billings, R.H., Schneider, H.M.: 'Water drop corona effects on full-scale 500 kV non-ceramic insulators', *IEEE Trans. PWD*, 1999, **14**, (1), pp. 999–1020

[35] Molinié, P., Goldman, M., Gatellet, J.: 'Surface potential decay on corona-charged epoxy samples due to polarization processes', *J. Phys. D, Appl. Phys.*, 1995, **28**, (8), pp. 1601–1610

[36] Kumara, S., Ma, B., Serdyuk, Y.V., *et al.*: 'Surface charge decay on HTV silicone rubber: effect of material treatment by corona discharges', *IEEE Trans. Dielectr. Electr. Insul.*, 2012, **19**, (6), pp. 2189–2195
[37] Meyer, L.H., Jayaram, S.H., Cherney, E.A.: 'A novel technique to evaluate the erosion resistance of silicone rubber composites for high voltage outdoor insulation using infrared laser erosion', *IEEE Trans. Dielectr. Electr. Insul.*, 2005, **12**, (6), pp. 1201–1208
[38] Sansonetti, J.E.,, Martin, W.C.: 'Handbook of basic atomic spectroscopic data', *J. Phys. Chem. Ref. Data*, 2005, **34**, pp. 1559–2259
[39] Zhang, S, Wang, X, He, M., *et al.*: 'Laser-induced plasma temperature', *Spectrochim. Acta B, At. Spectrosc.*, 2014, **97**, pp. 13–33
[40] Cowpe, J.S., Moorehead, R.D., Moser, D., *et al.*: 'Hardness determination of bio-ceramics using laser-induced breakdown spectroscopy', *Spectrochim. Acta B*, 2011, **66**, (3–4), pp. 290–294